Conformational heterogeneity determined by folding and oligomer assembly routes of the interferon response inhibitor NS1 protein, unique to human respiratory syncytial virus

Esteban Pretel[1], Ignacio E. Sánchez[2], Marisol Fassolari[1], Lucía B. Chemes[1] and Gonzalo de Prat-Gay[1,3*]

[1] Protein Structure-Function and Engineering Laboratory, Fundación Instituto Leloir and IIBBA-CONICET, Av. Patricias Argentinas 435, 1405 Buenos Aires, Argentina.

[2] Protein Physiology Laboratory, Departamento de Química Biológica, Facultad de Ciencias Exactas y Naturales and IQUIBICEN-CONICET, Universidad de Buenos Aires, Buenos Aires, Argentina.

[3] Ciência Sem Fronteiras Senior Fellow, CNPq, Laboratório de Genômica Estrutural, Instituto de Biofísica Carlos Chagas Filho, Universidade Federal do Rio de Janeiro, Rio de Janeiro, RJ, Brazil.

* Corresponding author: gpg@leloir.org.ar

Funding Source Statement

This work was supported by ANPCyT (Agencia Nacional de Promoción Científica y Tecnológica) PICT 2011-0721, CONICET (Consejo Nacional de Investigaciones Científicas y Técnicas) PIP 2011-2014, and by Ciência Sem Fronteiras (Rio de Janeiro, Brazil) Program Grants to GdePG. E.P. and M.F. are recipients of a CONICET predoctoral fellowship, and I.E.S., L.B.C. and G.deP.G are CONICET researchers.

ABBREVIATIONS

RSV: Respiratory Syncytial Virus

hRSV : Human Respiratory Syncytial Virus

IFN: Interferon

NS1SOS: NS1 Soluble spherical oligomers

CD: Circular Dichroism

ThT: Thioflavin T

ABSTRACT

The nonstructural NS1 protein is an essential virulence factor of the human respiratory syncytial virus, with a predominant role in the inhibition of the host antiviral innate immune response. This inhibition is mediated by multiple protein-protein interactions, and involves the formation of large oligomeric complexes. There is neither a structure nor sequence or functional homologues of this protein, which points to a distinctive mechanism for blocking the interferon response among viruses. The NS1 native monomer follows a simple unfolding kinetics via a native-like transition state ensemble, with a half-life of 45 minutes, in agreement with a highly stable core structure at equilibrium. Refolding is a complex process that involves several slowly interconverting species compatible with proline isomerization. However, an ultra-fast folding event of 0.2 milliseconds half-life is indicative of a highly folding compatible species within the undolded state ensemble. On the other hand, the oligomeric assembly route from the native monomer, which does not involve unfolding, shows a monodisperse and irreversible end-point species triggered by mild temperature change, with a half-life of 160 and 26 minutes at 37 and 47 degrees Celsius, respectively, and at low protein concentration (10 micromolar). A large secondary structure change into beta-sheet structure and the formation of a dimeric nucleus precedes polymerization by the sequential addition of monomers at the surprisingly low rate of one monomer every 34 seconds. The polymerization phase is followed by the binding to thioflavin-T indicative of amyloid-like, albeit soluble, repetitive beta sheet quaternary structure. The overall process is reversible only up until ~8 minutes, a time window where most of the secondary structure change takes place. NS1's multiple binding activities must accommodate in a few binding interfaces at most, something to be considered remarkable given its small size (15 KDa). Thus, conformational heterogeneity, and in particular oligomer formation, may provide a means to expand its binding repertoire. These equilibria will be determined by variables such as macromolecular crowding, protein-protein interactions, expression levels, turnover, or specific subcellular localization. The irreversible and quasi-spontaneous nature of the oligomer assembly, together with the fact that NS1 is the most abundant viral protein in infected cells, makes its accumulation highly conceivable in conditions compatible with the cellular milieu. The implications of NS1 oligomers in the viral life cycle and the inhibition of host innate immune response remain to be determined.

Keywords: NS1 protein, oligomer, human respiratory syncytial virus, folding kinetics, aggregation kinetics.

Paramyxoviruses are a diverse family of enveloped non-segmented negative-strand RNA viruses that belong to the order of Mononegavirales. Some of them are the most ubiquitous disease-causing viruses of humans and animals, including human parainfluenza viruses type 1 – 4, mumps, measles and other lethal zoonotic virues such as Nipah and Hendra from the Paramyxovirinae subfamily. Human Respiratory Sincytial Virus (hRSV), a member of the Pneumovirinae subfamily(*1*) , is the leading cause of lower respiratory tract disease among young children and immunocompromised individuals. hRSV infection is one of the most frequent reasons for hospitalization in developing countries, where 99% of hRSV related deaths take place (*2*) In addition, hRSV infection is believed to be associated to long-term complications, such as recurrent wheezing and asthma (*3*). Despite the fact that during the last decades there has been a significant progress in the understanding of hRSV pathogenesis, there is no antiviral treatment or effective vaccine available to date (*4, 5*).

Paramyxoviruses induce a wide variety of host responses upon infection. The first line of host defense against infection is the activation of the interferon (IFN) pathways. The IFN induction pathway is initiated by the activation of the RIG-I cytoplasmic RNA sensor, which recognizes viral RNA products (*6*). Through its CARD domain, RIG-I activates the signaling adaptor MAVS (*7*), located in the outer membrane of mitochondria. MAVS activation by RIG-I leads to polymerization of inactive MAVS monomers into functional amyloid-like oligomers docked on the surface of the mitochondrial membrane (*8*), which amplifies signaling of the IFN induction pathway and activates transcription of IFN-regulated genes. Produced IFN is secreted and is able to interact with IFN receptors, thus triggering the IFN response pathway. This signaling pathway promotes the phosphorylation

and activation of signal transducer and activation of transcription proteins (STAT 1 and 2), which translocate to the nucleus and lead to transcriptional activation of responsive genes encoding proteins with antiviral effects (*9, 10*).

To evade these antiviral defense mechanisms, Paramyxoviruses evolved different strategies, which result in a decreased IFN production or disruption of the IFN signaling pathways, leading to enhanced disease. Inhibition of IFN synthesis by Paramyxoviruses includes mechanisms such as the inhibition of cellular RNA sensors, control of aberrant viral RNA synthesis, signaling kinases or suppression of the IFN promoter. The mechanisms related to inhibition of IFN signaling include sequestration of signaling factors, upregulation of cellular inhibitory molecules or targeted degradation of signaling products (*11*). This inhibition of IFN signaling is mediated by the RSV non-structural (NS) proteins NS1 and NS2, which are unique to RSV and show no sequence homology to other known viral or cellular proteins, even within the Paramyxoviruses (*12*). The NS proteins have been shown to target different members of the interferon (IFN) induction and response pathways, decreasing levels of IFN α and β (*13-22*). NS2 was shown to interact with RIG-I, inhibiting RIG-I-MAVS binding and downstream signal transduction (*23*). Furthermore, in another report the interaction between MAVS and NS1 was investigated, and it was found that this binding interferes with the RIG-I-MAVS interaction, and that recombinant viruses lacking NS1 do not seem to affect this interaction (*15, 19, 24*). It was shown that NS proteins, predominantly NS2, decrease levels of STAT2 promoting its proteasomal degradation[12, 16,] (*25*). In addition, NS1 and NS2 may play a role in RNA replication, with a stronger inhibitory effect reported for NS1 in comparison with NS2 (*26*).

Given the relevance of NS1 and its uniqueness to RSV among all Paramyxoviruses, the lack of information on the structure and biochemical activity that underlies its

biological function is noticeable. Previously, others and we showed that the 15.5 KDa NS1 protein is a stable monomer in solution (*27, 28*). Chemical denaturation experiments showed that the NS1 monomer unfolds following a highly cooperative two-state and fully reversible reaction (*28*). However, under mild conditions compatible with the intracellular environment, conformational changes are induced, leading to the formation of large (~ 150 monomer units) soluble spherical oligomers (NS1SOs) as determined by atomic force microscopy and dynamic light scattering assays (*28*). These oligomers are highly stable and homogeneous species with similar size and shape in solution, and present repetitive beta-sheet structures which bind Congo Red and Thioflavin T dyes. Recent functional data suggests that NS1 oligomerization may be relevant *in vivo*. Namely, NS1 transfected in lung epithelial cells was shown to form homo-oligomers and to interact with NS2 (*20*). Moreover, a large heterogeneous protein complex called "degradosome" has been described, which has a molecular weight in the 300-750 KDa range and contains both NS1 and NS2 proteins as well as proteasome subunits. The degradosome presents degradative activity for many NS1 and NS2 cellular targets, such as RIG-I, TRAF3 and STAT2, and was found to be important in innate immunity suppression in infected cells (*29*). These findings could indicate that the NS1SOs formed quasi-spontaneously *in vitro*, could be correlated to the "degradosome" complex, and may represent a functionally relevant species in vivo.

In this work, with the goal of understanding the binding promiscuity of this unique protein, we set out to investigate the folding mechanism of the monomer and the assembly mechanism of the NS1 oligomer. Using different spectroscopic techniques, we found folding kinetics to be a complex process, in contrast to the simple two-state behavior shown at equilibrium and in unfolding kinetics. We dissected the oligomerization mechanism and

propose a model of NS1 self-assembly. After an initial step involving a reversible nucleation intermediate, the reaction proceeds irreversibly, leading to the formation of spherical particles. We discuss the results in connection with its known and hypothesized activities related to its capacity to inhibit interferon response.

EXPERIMENTAL PROCEDURES

Expression and purification of the hRSV NS1 protein. The human RSV strain A NS1 protein was recombinantly expressed and purified as previously described (*28*). Briefly, C41(DE3) cells harboring the plasmid pMal 2C, with the NS1 sequence cloned as a thrombin cleavage fusion protein to the maltose binding protein (MBP), were grown in LB medium at a DO of 0.6 and protein expression was induced with 0.3 mM IPTG, after which cells were incubated at 20°C for 16hs. The soluble protein was precipitated with 50% ammonium sulfate, resuspended, and purified with an affinity amylose resin (New England Biolabs, Hitchin, UK), followed by a thrombin treatment and a size exclusion chromatography to cleave and separate NS1 from the fusion protein MBP. Pure NS1 was dialyzed against 10 mM Tris-HCl buffer pH 8.0, 0.2 M NaCl, and 1 mM DTT. Protein concentration was determined spectrophotometrically using a molar extinction coefficient of $\varepsilon_{280\,nm} = 9970\ M^{-1}\ cm^{-1}$.

Circular dichroism and fluorescence spectroscopy. Far-UV Circular Dichroism (CD) measurements were performed on a Jasco J-810 spectropolarimeter using a Peltier temperature-controlled sample holder at 20 °C. Spectra were recorded between 200 and 260 nm at a scan rate of 100 nm/min, with a response time of 4 s and a bandwidth of 2 nm. All spectra were an average of at least four to six scans. Raw data were converted to molar ellipticity using the following equation:

$$[\theta] = \frac{\text{deg}}{[c] \cdot \#bonds \cdot L \cdot 10,000} \quad (1)$$

where, deg is the raw signal in millidegrees, [c] is protein concentration in molar units, #bonds is the number of peptide bonds, and L is the path length in cm.

Folding kinetics

Fluorescence experiments were performed in a Jasco FP-6500 spectrofluorometer. In all cases an excitation bandwidth of 1 nm and emission bandwidth of 20 nm were used in order to minimize bleaching and to maximize signal to noise ratio. Temperature was controlled by a peltier device coupled to the measurement cell.

Unfolding kinetics. Native protein from a concentrated stock solution was diluted 10-fold by manual mixing into 10 mM Tris-HCl pH 8.0, 200 mM NaCl, and 1 mM DTT buffer with the indicated amount of Gdm.Cl, to a final protein concentration of 8 μM. CD kinetics were monitored at 216 nm, with a bandwidth of 10 nm and a response time of 4 s. A decrease in the ellipticity signal was measured until a steady state was reached. Fluorescence kinetics were monitored by measuring NS1 fluorescence, originated by its single tryptophan (Trp) residue, with an excitation wavelength of 295 nm and an emission wavelength of 325 nm. The fluorescence change (decrease) was measured until a steady state was reached. In all experiments temperature was kept constant at 20 °C.

Refolding kinetics. Unfolded NS1 from a concentrated stock solution, equilibrated for at least 3 hours in 5 M Gdm.Cl , was diluted 10-fold by manual mixing into 10 mM Tris-HCl pH 8.0, 200 mM NaCl, and 1 mM DTT buffer with the indicated amount of Gdm.Cl, to a final protein concentration of 8 μM. Fluorescence kinetics were monitored with the same parameters described for unfolding with a resultant increase in Trp fluorescence.

Stoppped-flow kinetics. Refolding kinetics were measured in a SX18MV stopped-flow apparatus (Applied Photophysics, Leatherhead, UK) by diluting equilibrated fully unfolded protein from a concentrated (60 μM) stock solution in 5 M Gdm.Cl, 10mM Tris-HCl

buffer, pH 8.0, 200 mM NaCl and 1mM DTT 10-fold, into the same buffer with the indicated amount of Gdm.Cl. The final protein concentration throughout the experiments was 6μM. The excitation wavelength was 280 nm and a 320 nm emission high-pass filter was used.

Folding data analysis. The observed rate constants for each folding or unfolding reaction were obtained by fitting the kinetic traces, as required, to an equation containing up to three exponential functions:

$$F(t) = \sum A_n \exp(-k_n t) + F_\infty \quad (2)$$

Where, $F(t)$ and F_∞ are the observed signal at time t and at infinite time, respectively. A_n and k_n are the signal amplitude and rate constants respectively, for each process. Fitting was performed using the ProFit sofware (Quantumsoft, Zurich). The criteria followed to choose the minimal number of exponentials providing the best fit for each trace was: 1) random dispersion of residuals; 2) low standard deviation values (at most 1/5 of the parameter value for rate constants); 3) significant improvement of the fit Chi-square values (in relation to an equation with simpler parameters). When treating refolding data, 3 phases were observed for all refolding reactions, in both slower time-scale manual mixing and faster time-scale stopped flow experiments time scales. As the slowest phase from stopped flow experiments and the fastest phase from manual mixing refolding experiments shared similar rate constants, we performed a global fit of manual mixing and stopped flow refolding traces for most Gdm.Cl concentrations tested. All traces were normalized prior to fitting.

Following trace fitting, the natural logarithm of the observed rate constants as a function of Gdm.Cl concentration was plotted to obtain a Chevron Plot for NS1 folding. Assuming a two state model for NS1 folding, the following relationships between equilibrium and

kinetic constants can be obtained (*30*):

$$U \underset{k_u}{\overset{k_f}{\rightleftharpoons}} N \quad (3)$$

$$K_{eq} = k_f / k_u \quad (4)$$

where, U and N are the unfolded and native states, respectively, K_{eq} is the folding equilibrium constant, and k_f and k_u are the microscopic rate constants for folding and unfolding respectively.(*30*) K_{eq} for NS1 was previously reported, obtaining a value of 6.48 x 10^{-8} (*28*). The k_u was obtained from the Chevron Plot, by extrapolating the value of ln k_{obs} at 0 M Gdm.Cl from a linear fit of the unfolding limb, which showed a linear dependence on [Gdm.Cl] (*30*). Using the two state model described in Eq. 3 and Eq. (4) we calculated k_f from K_{eq} and k_u. The m_{eq} value is a measure of the dependence of the free energy of refolding on denaturant concentration (*30*), and was previously reported for NS1, obtaining a value of 2.5 kcal·mol^{-1}·M^{-1} (*28*). The m_{eq} values were shown empirically to be proportional to changes in accessible surface area (ΔASA) of the native state of a protein upon unfolding (*31*). Similarly, kinetic *m* values describe the dependence of the activation free energy for folding and unfolding reactions on denaturant concentration. The kinetic $m_u^{\ddagger}$ value is considered to reflect changes in ΔASA between the native state and the transition state ensemble (*30*), while the $m_f^{\ddagger}$ value reflects changes in ΔASA from the unfolded state to the transition state ensemble. The $m_u^{\ddagger}$ value was obtained from the Chevron Plot, as the slope of the linear fit of the unfolding limb multiplied by *RT*, where *R* is the gas constant (1.9872 x10^{-3} kcal·mol^{-1}) and *T* is the temperature of the experiment in ºK. Following the two state model, m_{eq} is related to $m_f^{\ddagger}$ and $m_u^{\ddagger}$ as follows (*30*),

$$m_{eq} = m_u^{\ddagger} - m_f^{\ddagger} \quad (5)$$

therefore, we calculated $m_f^{\ddagger}$ using equation (5) and the obtained values of m_{eq} and $m_u^{\ddagger}$. In order to gain information about burial of accessible surface area in the transition state, we calculated an alpha value, as follows (*32*):

$$\alpha = 1 - \frac{m_u^{\ddagger}}{m_{eq}} \qquad (6)$$

Oligomerization kinetics

Oligomerization was followed by monitoring changes in the far UV-CD signal at 220 nm or in Thioflavin T fluorescence following transfer of Monomeric NS1 from a concentrated stock solution held at 4 °C to a cuvette containing 10 mM Tris-HCl buffer pH 8.0 and 1 mM DTT, maintained at the indicated temperature in each experiment. The concentration dependence of the reaction was measured by varying NS1 concentration from 2.5 to 10 μM at 47 °C. The oligomerization reaction was additionally measured by following the increase in ThT fluorescence with time after concentrated NS1 was transferred to a cuvette containing buffer equilibrated with a final ThT final concentration of 20 μM. We previously showed that monomeric NS1 does not bind ThT, while NS1 oligomers do bind ThT (*28*). Therefore, the ThT fluorescence increase was used as a proxy of NS1 oligomerization. The excitation wavelength in these experiments was 446 nm, and signal changes were monitored at 490 nm, using an excitation bandwidth of 1 nm and an emission bandwidth of 20 nm.

Dinamic light scattering. The particle size distribution for NS1 samples was obtained using a Zetasizer Nano S DLS device from Malvern Instruments (Malvern). NS1 protein was filtered with Ultrafree-MC microcentrifuge 0.22 μm filters (Millipore) before measurements were done. NS1 protein at 17 μM in buffer containing 10 mM Tris-HCl with

1 mM DTT was incubated at 40 ºC (controlled by Peltier control system) and time-dependent changes in particle size diameter were followed. Each measurement was an average from 10 scans of 10 seconds each.

Temperature-jump experiments. NS1 from a stock solution held at 4 °C, was transferred to 10 mM Tris.Cl buffer, pH 8.0 and 1 mM DTT at 47 °C with a final protein concentration of 12 μM. After a delay time ranging from 50 to 2000 s, samples were transferred to a sample cell holder kept at 20 °C and the far UV-CD signal at 220 nm was monitored. After a steady-state was reached, Far UV-CD spectra were measured, and samples were run in a gel filtration S-75 column.

Size exclusion chromatography. Size exclusion chromatography experiments were carried out on a Superdex 75 HR 10/30 column (24 mL) at a flow rate of 0.5 ml/min. The column was calibrated with ovalbumin (44.2 KDa), chymotrypsinogen A (25 KDa), and ribonuclease A (13.7 kDa). The void volume (V_0) and total volume (V_t) were determined by loading Blue Dextran and acetone, respectively. The buffer used was Tris-HCl 10 mM pH 8.0 and DTT 1 mM with a protein concentration of 12 μM at 20 °C.

Oligomerization data analysis. Traces from concentration dependence experiments were normalized and used for model analysis. For nucleus size determination we used a kinetically limited model, developed by Zlotnick *et al*. (*33*):

$$\log\left[NS1SOs\right] = \log k + n \cdot \log\left[NS1_{monomer}\right] \quad (7)$$

where *k* is a proportionality constant and n is the size of the nucleus. The ThT fluorescence was used as a proxy of NS1SOs assembly. The [*NS1SOs*] and [$NS1_{monomer}$] represent the concentration of NS1 oligomers and monomers, respectively and were calculated at five

different time points during the exponential phase (ranging 200 and 600 s). At each time point and concentration, we defined [NSISOs] = [NS1 total concentration] x normalized ThT fluorescence signal and [NS1 monomer] = [NS1 total concentration] x (1- normalized ThT fluorescence signal). These parameters were used to create a log-log plot. The size of the nucleus was then estimated from averaging the slope of the log-log plot of [NS1SOs] versus [NS1 monomer] for all curves. The obtained value was an average of the values obtained from the different time point datasets analyzed. The elongation rate constant for each trace was determined from the slope of the traces centered at 25% signal saturation. The order of the assembly reaction was determined from the slope of a log-log plot of the rate constants versus total NS1 concentration, as follows:

$$\log(elongation\ rate) = l\ x\ \log[NS1_{total}] + C \quad (8)$$

where $NS1_{Total}$ is the NS1 total concentration, l is the order of the reaction and C is a constant (*34*).

RESULTS

NS1 shows a simple unfolding kinetics

We previously showed that NS1 unfolds in a highly cooperative manner at equilibrium, following a two state and fully reversible reaction characterized by a concomitant loss of secondary and tertiary structure, with $\Delta G^{H2O}_{N\text{-}U}$ and m_{eq} values of 9.6 ± 0.9 kcal·mol^{-1} and 2.5 kcal·mol^{-1}·M^{-1}, respectively (*28*). As part of the dissection of the folding mechanism, we tackled a kinetic investigation. We started by studying NS1 unfolding kinetics by following changes in exposure of its single solvent-protected tryptophan residue (indicative of global tertiary structure unfolding), and also by monitoring changes in NS1 secondary structure upon Gdm.Cl denaturation through Far-UV Circular Dichroism (CD) measurements. As unfolding was a slow process, we performed manual mixing experiments, where native NS1 from a concentrated stock solution was diluted 10-fold into buffer solutions containing Gdm.Cl at a final concentrations ranging between 3.75 and 7.0 M (pH 8.0), and followed the resulting kinetic signals over time (see Materials and Methods).

Unfolding proved to be a rather simple process at all Gdm.Cl concentrations tested, and data analysis showed that at low and moderate Gdm.Cl concentrations (from 3.75 to 7.0 M) unfolding traces could be fitted to a single exponential function (Figure 1 and Supplementary Figure 1 and 2). At 5.0 M Gdm.Cl, the observed rate constant was (1.80 ± 0.02) x 10^{-3} s^{-1}, indicating a half-life of ~ 6 minutes for the unfolding reaction. The presence of a single observed rate constant in this Gdm.Cl concentration range indicated that only two species were populated in the unfolding reaction, the native state and the unfolded state. For all Gdm.Cl concentrations tested, changes in secondary and tertiary structure were superimposable processes and yielded similar rate constants (Figure 1). As an

example, at 6.0 M Gdm.Cl, data fitting yielded the following rate constants for unfolding: (2.89 ± 0.02) x 10^{-3} s^{-1} and (2.97 ± 0.02) x 10^{-3} s^{-1} for fluorescence and CD experiments, respectively.

The amplitudes and end points of the observed rate constants, from data fitting for fluorescence and CD unfolding experiments, were used to create a plot of initial and final values of the signals (Figures 2A and B). This analysis showed an excellent superposition between equilibrium and kinetic unfolding data, and also indicated that the observed amplitudes could account for the full change in each signal. These results indicate the absence of rapid processes (burst phase) during the experimental mixing dead time. The observed rate constants from fluorescence experiments as a function of Gdm.Cl concentration were plotted to create a Chevron Plot. For unfolding, we observed a linear dependence of the logarithm of the observed rate constant on guanidinium concentrations for most of the concentrations tested (Figure 3). We calculated the unfolding rate constant (k_u) at 0 M Gdm.Cl by extrapolation of a linear regression of the observed rate constants (from 5.0 - 7.0 M Gdm.Cl), obtaining a value of 2.5 ± 0.5 ·10^{-4} s^{-1}, and a value of 0.24 ± 0.02 kcal·mol^{-1}·M^{-1} for $m_u^{\ddagger}$ (Figure 3, see Materials and Methods).

NS1 unfolding can thus be described as a slow single exponential decay that accounts for the full change in fluorescence and CD signal between the native and the unfolded states. Kinetics recorded by CD and fluorescence are superimposable at all GdmCl concentrations tested, and the GdmCl dependence of the logarithm of the observed rate constant is linear. From this evidence, we can describe NS1 unfolding as a two-state process without populated intermediates.

Complex multiphasic refolding kinetics

Refolding was initially investigated by manual mixing and stopped-flow techniques as it proved to be a multi-phasic process with both several slow phases (minute time-scale) as well as rapid phases (seconds time-scale) that could not be measured by manual mixing (15 s). For both sets of experiments, concentrated and unfolded protein was diluted 10-fold in the appropriate buffer to reach final Gdm.Cl concentrations ranging from 0.5M to 3.5M. In both cases, the refolding process was followed by measuring changes in Trp fluorescence (see Materials and Methods).

Traces from stopped-flow experiments performed at 1M Gdm.Cl concentration, were best fitted to three exponential functions (Figure 4A), as was the case for most of the Gdm.Cl concentrations tested (see Supplementary Figure 3). Fitting of kinetic data from manual mixing experiments at 1M Gdm.Cl concentration, also showed the presence of 3 phases (Figure 4B), as did most of the Gdm.Cl concentrations tested (see Supplementary Figure 4). As a result, data yielded 6 observed rate constants. At all Gdm.Cl concentrations tested, the slowest phase measured by stopped flow techniques had a similar rate constant to the fastest phase measured by manual mixing experiments. For example, at 1.0 M Gdm.Cl these phases yielded the following rate constants: k_3 (7.0 ± 0.3) x 10^{-2} s^{-1} for stopped flow experiments and k_1 (3.8 ± 0.2) x 10^{-2} s^{-1} for manual mixing experiments, which indicated that this phase corresponded to the same event. We performed a global fit of the stopped flow and manual mixing refolding data (see Materials and Methods and Supplementary Figure 5), and based on this analysis, 5 phases could be well discriminated, with observed rates ranging from 0.75 ± 0.03 s^{-1} for the fastest phase to (1.90 ± 0.27) x 10^{-3} s^{-1} for the slowest phase at 1.0 M Gdm.Cl (Table 1). The presence of 5 phases indicated the population of at least 4 intermediate species in the refolding process (*30, 35*).

The amplitude analysis from refolding experiments was not performed due to instability of the stopped flow fluorescence signal in order to obtain a base line of the native and unfolded states. Therefore, the absence of a burst phase in the folding reaction could not be established. The resulting chevron plot from refolding experiments revealed that most phases presented a very low dependence on Gdm.Cl concentration (Figure 3), suggesting that they do not appear to represent major folding events. Remarkably, despite the fact that NS1 was previously found to undergo oligomerization under mild changes in solvent conditions (*28*), we found no dependence on protein concentration for either of the refolding rates (assessed in the 1 to 15 μM range for manual mixing and in the 1 to 10 μM range for stopped flow experiments, not shown), indicating that they did not reflect oligomerization events.

Taken together, these experiments allow us to conclude that, unlike unfolding, refolding is a complex reaction limited by slow unimolecular processes whose rates display low dependence on guanidinium concentration. The values of the rate constants, together with their low Gdm.Cl dependence are compatible with the rates associated with prolyl isomerization in the unfolded state, which are within the range of 0.001 and 0.1 s^{-1}(*36*). This suggests that the observed rate limiting steps in NS1 refolding could be due to Xaa-prolyl isomerization of one or more of its four proline residues (*37-39*), although further experiments are needed to confirm this hypothesis.

Kinetic dissection of NS1 oligomerization

We have previously shown that NS1 readily forms soluble and well defined oligomers (NS1SOs) upon mild modifications in the milieu (*28*). NS1SOs formation is accompanied by a substantial change in NS1 secondary structure, with an increase in β-

sheet content (Figure 5A, inset) (*28*). Moreover, NS1SOs were found to share features similar to amyloid-like or repetitive β-sheet structures, such as Thioflavin T and Congo Red binding (*28*). In order to investigate the mechanism of this quasi-spontaneous NS1 oligomerization pathway, we performed a kinetic study using ThT fluorescence, dynamic light scattering (DLS) and circular dichroism.

NS1 was stable at 20 ºC, whereas transfer to temperatures over 40 ºC led to NS1SOs formation (Figure 5). The formation of NS1SOs was triggered by a temperature-jump. In a first experiment, the assemble process was monitored by the increase in ThT fluorescence with time, after native NS1 held a 4 ºC was transferred to a buffer solution equilibrated at 40 ºC. A slow increase in ThT binding was observed, indicative of the formation of quaternary structure containing repetitive β-strands (Figure 5A). In a parallel experiment, we used DLS for monitoring the particle size diameter of native NS1 held at 4 ºC after transfer to a cell holder maintained at 40 ºC (Figure 5B, ○). The initial species showed an average particle size diameter of 4.2 nm and at the end point of the kinetics the particle size diameter was 24.4 nm, in excellent agreement with the previously described monomeric and oligomeric species (*28*) (Figure 5B, inset). The process showed multiple phases, with a noticeable lag-phase that preceded ThT fluorescence increase within the first 100 seconds. This lag phase was also evident when monitoring the particle size increase by DLS as the reaction proceeded, indicating the presence of intermediate species prior to oligomer formation (Figure 5B). Interestingly, Far-UV CD showed that changes in NS1 secondary structure took place before oligomer formation (Figure 5A), further supporting the presence of intermediate protein concentration independent species in the oligomerization process.

Defining nucleation and elongation steps in NS1SOS assembly

Next, in order to further dissect the mechanism of NS1 oligomerization we analyzed time-dependent changes of ThT fluorescence at varying protein concentrations, where native NS1 held at 4 ºC was transferred to buffer equilibrated at 47 ºC, and the resulting kinetics was measured by ThT fluorescence increase. Temperature was chosen in order to optimize the time window for data analysis, with protein concentrations ranging from 2.5 to 10 μM (Figure 6A). Normalization of the data showed protein concentration-dependent kinetics, as expected for a polymerization reaction (Figure 6A). To characterize the process, we used an oligomerization model developed by Zlotnick et al. (*33*) used to describe sigmoidal assembly kinetics in which there are three well defines phases, namely a lag-phase, an elongation phase and a final stationary phase. In this model, the lag phase can be correlated to nucleus formation, where the nucleus is defined as the minimal assembly unit (*40*). The ThT fluorescence kinetic data were normalized and used as a estimate of NS1SOs concentration (Figure 6A). At different time-points during the exponential phase (Figure 6A, grey zone) the [NS1SOs] and [NS1 monomer] for all concentrations tested were calculated (Figure 6B). The double log plot of [NS1SOs] as a function of [NS1 monomer] allows for nucleus size determination (Figure 6B, see Materials and Methods), where we calculated a nucleus size of 2.3 ± 0.3 NS1 molecules as an average value from the slope of 5 different time point datasets. These results indicated that the nucleus for NS1 oligomerization is a dimeric species. In addition, the order of the elongation reaction was determined from the slope of the log-log plot of the rate of NS1SOs formation as a function of NS1 total concentration (Figure 6C, see Materials and Methods). A value of 1.10 ± 0.06 NS1 molecules was obtained, clearly indicative of a first-order reaction, where oligomerization proceeds, through addition of monomers to the dimeric nucleus.

Partial reversibility of intermediate stages in NS1SOS assembly

As we previously described, the overall oligomerization reaction is an irreversible process (*28*). However, an important goal is to determine when this irreversibility takes place, and which intermediate events in NS1SOS assembly remain reversible. We tackled this issue by performing a double temperature-jump experiment in which native NS1 was transferred to 47 ºC, and at different time intervals the oligomerization reaction was stopped by transfer to 20 ºC while monitoring far UV-CD ellipticity at 220 nm (Figure 7A). The oligomerization process was characterized by an increment in negative ellipticity at 220 nm, from -5500 to -8500 $deg \cdot cm^2 \cdot dmol^{-1}$ (Figure 7B). Interestingly, we found that at short time delays cooling back led to recovery of the initial ellipticity signal, yielding steady state values equal to those of the NS1 monomer. The final species obtained at the end point after the temperature-jump at 50 seconds had an identical Far UV-CD spectrum to that of native NS1 (Figure 8A), indicating that at early stages the oligomerization process was reversible. At longer time delays this reversibility was slowly lost, as indicated by a lack of full recovery of the CD signal, which takes place between 320 and 480 seconds (Figure 7B). To verify these results, we performed a similar experiment where the oligomerization state of the final species formed was monitored using size exclusion chromatography, performed at the end of each experiment after transfer back to 20 ºC (Figure 7A and 8B). At 50 and 100 second delays we did not detect significant oligomer formation confirming the full reversibility of the process as observed by CD, and monomeric native NS1 was recovered. In agreement with the CD kinetic experiment, there was a gradual accumulation of oligomeric species which eluted in the void volume of the column after transfer back to 20 ºC at longer time delays, and this accumulation proved to be highly superimposable with the oligomerization reaction followed by ThT fluorescence

(Figure 8C).

DISCUSSION

The NS1 protein from Human Respiratory Syncytial Virus is considered as one of the main RSV virulence factors, having a central role in innate immunity inhibition. Despite its relevance, little is known about the molecular mechanisms involved in this immune evasion process. In addition, the absence of an effective vaccine or antiviral treatment evidences the requirement of detailed mechanistic information since biophysical information is scarce and the structure and biophysical properties of this protein have not been elucidated to date. Previously, we showed that NS1 can populate several conformational states at equilibrium, including the native and unfolded monomers, and spherical oligomeric species(*28*). In order to characterize the dynamics of interconversion among these species, we performed kinetic measurements of folding and temperature induced oligomerization.

Figure 9 shows a summary of NS1 diverse stable species in solution, and the transitions between them. Kinetic unfolding of the native state *N* is a two-state process with a half-time of 46 minutes, which indicates a high kinetic stability of the native monomer. In addition, the denaturant dependence of the unfolding kinetics and equilibrium allow us to characterize the transition state for the unfolding reaction. We used the corresponding *m* values to calculate an alpha value ($\alpha = 1 - (m_u/m_{eq})$, see Materials and Methods) (*31, 32*). The alpha value can be interpreted as the relative amount of accessible surface area in the transition state ensemble. In the simplest case, this parameter takes values between 0 and 1, where 1 indicates a native-like accessible surface area in the transition state, and 0 indicates an unfolded-like accessible surface area in the transition state. We obtained an alpha value

of 0.90 ± 0.02, indicative of a transition state ensemble for unfolding with native-like solvent accessibility.

Based on our refolding experiments, we propose a minimal model for NS1 folding (Figure 9, left hand side). According to this model, formation of a folding-competent species (U_{Fast}), which has all its Xaa-proline residues in their yet unknown native conformation, is limited by slow equilibria with unfolded NS1 monomers containing one or more non-native prolyl isomers (U_{Slow} species). Assuming that the four NS1 prolines populate the *trans* isomer in the native state, statistically at least 35% of unfolded molecules would present a non-native peptide bond at equilibrium (*36*). If one of the prolines populates the *cis* isomer in the native state, this percentage would rise to 92% (*36*). It remains intriguing whether NS1 molecules with non-native peptide bonds can fold or function to a significant degree. We may also consider the folding rate of the folding-competent U_{Fast} species. We estimated the value of the main refolding rate constant combining data measured from unfolding kinetics with previously reported equilibrium data (*28*). This yielded a k_f value of 3860 ± 850 s^{-1}, and an $m_f^{\ddagger}$ value of -2.26 ± 0.20 $kcal \cdot mol^{-1} \cdot M^{-1}$ (Figure 3 discontinuous line, and see Materials and Methods), indicating that the highly competent U_{Fast} folding species has a very short half-life (0.2 milliseconds), and rapidly yields the native state *N*.

The right-hand side of Figure 9 shows a model for NS1SOS assembly. Oligomerization kinetics follow a sequential process, where the main events are represented by a lag-phase, an elongation phase and a stationary phase (Figure 5), features which are typical of nucleation-limited polymerization reactions. During the lag-phase no oligomers are formed (Figure 5B), but substantial secondary structure changes in the native NS1 monomer *N* take place in the minutes time-scale (Figure 5A) to form a non-native monomer

*M** (Figure 9). Data fitting from CD experiments at 10 μM using a single exponential decay allowed us to estimate the time constant of this step obtaining a half time of 3.8 minutes (Figure 9). During the lag phase, conformational changes are reversible, and the native monomer *N* can be recovered upon cooling (Figures 7 and 8). After the dimeric nucleus *M2** is formed during the lag phase, most if not all of the secondary structure change has taken place (Figures 5A and 6B). This event is followed by the sequential addition of monomers (Figure 6C and 8), which becomes irreversible between 320 and 480 seconds at 10μM protein concentration (Figure 7B). In these conditions at 47 ºC, NS1SOs assembly is complete within 83 minutes (Figure 6A). Using the estimated number of monomers in NS1SOs of 149 (*28*), we estimate that during polymerization one NS1 monomer will be added on average to the oligomer every 34 seconds (Figure 9).

Previous work has described the presence of NS1 oligomers in transfected and infected cells as well as large functional complexes with other proteins (*20, 29*). For example, the RSV NS degradosome was shown to be heterogeneous in size (300-750 KDa) and proposed to include the viral NS1 and NS2 proteins as well as host proteasome subunits. The size of the degradosome is compatible with the presence of NS1 oligomers within it. Suppression of the innate immune response in HRSV infected cells is mediated by interactions between the NS degradosome and a large oligomeric assembly of MAVS proteins on the mitochondrial membrane, which enhances viral degradative activity (*29*). The mitochondrial signaling protein (MAVS) oligomerizes following viral infection, forming active amyloid type polymers that amplify IFN signaling (*8*). Moreover, electron microscopy studies showed that NS1 and MAVS co-localize, suggesting that both proteins may mediate the interaction between the NS degradosome and the MAVS assembly (*24*). If this is the case, NS1 oligomerization may act as a scaffold for degradosome assembly as

well as for interaction with MAVS, making NS1 oligomerization a plausible drug target for suppressing viral shutdown of the host innate immune response.

In summary, here we describe diverse but discrete states of RSV NS1 in solution that may help us understand its multiple binding activities reported (20-22), especially so in the absence of structural information, homologs, or functionally related proteins within paramyxoviruses. These multiple binding activities must accommodate in a few binding interfaces at most, something unlikely to be specific given its small size (15 KDa). This strongly suggests that conformational heterogeneity, and in particular oligomer formation, may provide a necessary means to expand the NS1 binding repertoire.

The different species described herein interconvert in the minutes to hours timescale, implying that even if they are present at low concentrations, variables such as macromolecular crowding, protein-protein interactions or specific subcellular localization may alter the equilibria and dynamics of these processes leading to their accumulation. The irreversible and quasi-spontaneous nature of the NS1SOs assembly in mild temperature conditions, together with the fact that it is the most abundant viral protein in RSV-infected cells, turns its accumulation highly conceivable. This work should be extended to the investigation of oligomers in infected cells and their functional implications in the viral life cycle and in the inhibition of host innate immune response.

Supporting Information

Supporting information available includes Supplementary Figures S1-S5.

REFERENCES

1. Lamb, R. A., Parks, G.D. . (2007) Paramyxoviridae: The viruses and Their Replication, in *Fields in Virology* (Knipe D.M., H. P. M., Ed.), Lippincott Williams & Wilkins, Philadelphia. Vol 1, Ch 41: pp 1449-1496.
2. Welliver, R. C. (2004) Respiratory syncytial virus infection: therapy and prevention, *Paediatr Respir Rev 5 Suppl A*, S127-133.
3. Jafri, H. S., Chavez-Bueno, S., Mejias, A., Gomez, A. M., Rios, A. M., Nassi, S. S., Yusuf, M., Kapur, P., Hardy, R. D., Hatfield, J., Rogers, B. B., Krisher, K., and Ramilo, O. (2004) Respiratory syncytial virus induces pneumonia, cytokine response, airway obstruction, and chronic inflammatory infiltrates associated with long-term airway hyperresponsiveness in mice, *J Infect Dis 189*, 1856-1865.
4. Empey, K. M., Peebles, R. S., Jr., and Kolls, J. K. (2010) Pharmacologic advances in the treatment and prevention of respiratory syncytial virus, *Clin Infect Dis 50*, 1258-1267.
5. Collins, P. L., and Melero, J. A. (2011) Progress in understanding and controlling respiratory syncytial virus: still crazy after all these years, *Virus Res 162*, 80-99.
6. Myong, S., Cui, S., Cornish, P. V., Kirchhofer, A., Gack, M. U., Jung, J. U., Hopfner, K. P., and Ha, T. (2009) Cytosolic viral sensor RIG-I is a 5'-triphosphate-dependent translocase on double-stranded RNA, *Science 323*, 1070-1074.
7. Kawai, T., Takahashi, K., Sato, S., Coban, C., Kumar, H., Kato, H., Ishii, K. J., Takeuchi, O., and Akira, S. (2005) IPS-1, an adaptor triggering RIG-I- and Mda5-mediated type I interferon induction, *Nat Immunol 6*, 981-988.
8. Hou, F., Sun, L., Zheng, H., Skaug, B., Jiang, Q. X., and Chen, Z. J. (2011) MAVS forms functional prion-like aggregates to activate and propagate antiviral innate immune response, *Cell 146*, 448-461.
9. Basler, C. F., and Garcia-Sastre, A. (2002) Viruses and the type I interferon antiviral system: induction and evasion, *Int Rev Immunol 21*, 305-337.
10. Randall, R. E., and Goodbourn, S. (2008) Interferons and viruses: an interplay between induction, signalling, antiviral responses and virus countermeasures, *J Gen Virol 89*, 1-47.
11. Parks, G. D., and Alexander-Miller, M. A. Paramyxovirus activation and inhibition of innate immune responses, *J Mol Biol 425*, 4872-4892.
12. Collins, P. L., and Crowe, J. E. (2007) Respiratory syncytial virus and metapneumovirus, in *Fields Virology* (Knipe, D. M., Howley,, and P.M., Eds.), pp 1601-1646, Lippincott Williams & Wilkins, Philadelphia.
13. Spann, K. M., Tran, K. C., Chi, B., Rabin, R. L., and Collins, P. L. (2004) Suppression of the induction of alpha, beta, and lambda interferons by the NS1 and NS2 proteins of human respiratory syncytial virus in human epithelial cells and macrophages [corrected], *J Virol 78*, 4363-4369.
14. Spann, K. M., Tran, K. C., and Collins, P. L. (2005) Effects of nonstructural proteins NS1 and NS2 of human respiratory syncytial virus on interferon regulatory factor 3, NF-kappaB, and proinflammatory cytokines, *J Virol 79*, 5353-5362.

15. Lo, M. S., Brazas, R. M., and Holtzman, M. J. (2005) Respiratory syncytial virus nonstructural proteins NS1 and NS2 mediate inhibition of Stat2 expression and alpha/beta interferon responsiveness, *J Virol 79*, 9315-9319.
16. Bossert, B., and Conzelmann, K. K. (2002) Respiratory syncytial virus (RSV) nonstructural (NS) proteins as host range determinants: a chimeric bovine RSV with NS genes from human RSV is attenuated in interferon-competent bovine cells, *J Virol 76*, 4287-4293.
17. Ramaswamy, M., Shi, L., Varga, S. M., Barik, S., Behlke, M. A., and Look, D. C. (2006) Respiratory syncytial virus nonstructural protein 2 specifically inhibits type I interferon signal transduction, *Virology 344*, 328-339.
18. Gotoh, B., Komatsu, T., Takeuchi, K., and Yokoo, J. (2001) Paramyxovirus accessory proteins as interferon antagonists, *Microbiol Immunol 45*, 787-800.
19. Swedan, S., Musiyenko, A., and Barik, S. (2009) Respiratory syncytial virus nonstructural proteins decrease levels of multiple members of the cellular interferon pathways, *J Virol 83*, 9682-9693.
20. Swedan, S., Andrews, J., Majumdar, T., Musiyenko, A., and Barik, S. (2011) Multiple functional domains and complexes of the two nonstructural proteins of human respiratory syncytial virus contribute to interferon suppression and cellular location, *J Virol 85*, 10090-10100.
21. Wu, W., Tran, K. C., Teng, M. N., Heesom, K. J., Matthews, D. A., Barr, J. N., and Hiscox, J. A. (2012) The interactome of the human respiratory syncytial virus NS1 protein highlights multiple effects on host cell biology, *J Virol 86*, 7777-7789.
22. Hastie, M. L., Headlam, M. J., Patel, N. B., Bukreyev, A. A., Buchholz, U. J., Dave, K. A., Norris, E. L., Wright, C. L., Spann, K. M., Collins, P. L., and Gorman, J. J. (2012) The human respiratory syncytial virus nonstructural protein 1 regulates type I and type II interferon pathways, *Mol Cell Proteomics 11*, 108-127.
23. Ling, Z., Tran, K. C., and Teng, M. N. (2009) Human respiratory syncytial virus nonstructural protein NS2 antagonizes the activation of beta interferon transcription by interacting with RIG-I, *J Virol 83*, 3734-3742.
24. Boyapalle, S., Wong, T., Garay, J., Teng, M., San Juan-Vergara, H., and Mohapatra, S. (2012) Respiratory syncytial virus NS1 protein colocalizes with mitochondrial antiviral signaling protein MAVS following infection, *PLoS One 7*, e29386.
25. Elliott, J., Lynch, O. T., Suessmuth, Y., Qian, P., Boyd, C. R., Burrows, J. F., Buick, R., Stevenson, N. J., Touzelet, O., Gadina, M., Power, U. F., and Johnston, J. A. (2007) Respiratory syncytial virus NS1 protein degrades STAT2 by using the Elongin-Cullin E3 ligase, *J Virol 81*, 3428-3436.
26. Atreya, P. L., Peeples, M. E., and Collins, P. L. (1998) The NS1 protein of human respiratory syncytial virus is a potent inhibitor of minigenome transcription and RNA replication, *J Virol 72*, 1452-1461.
27. Ling, Z., Tran, K. C., Arnold, J. J., and Teng, M. N. (2008) Purification and characterization of recombinant human respiratory syncytial virus nonstructural protein NS1, *Protein Expr Purif 57*, 261-270.
28. Pretel, E., Camporeale, G., and de Prat-Gay, G. (2013) The non-structural NS1 protein unique to respiratory syncytial virus: a two-state folding monomer in quasi-equilibrium with a stable spherical oligomer, *PLoS One 8*, e74338.

29. Goswami, R., Majumdar, T., Dhar, J., Chattopadhyay, S., Bandyopadhyay, S. K., Verbovetskaya, V., Sen, G. C., and Barik, S. (2013) Viral degradasome hijacks mitochondria to suppress innate immunity, *Cell Res 23*, 1025-1042.
30. Buchner, J., and Kiefhaber, T. (2005) *Protein folding handbook*, Vol. 3: 379-410, Weinheim: Wiley-VCH.
31. Myers, J. K., Pace, C. N., and Scholtz, J. M. (1995) Denaturant m values and heat capacity changes: relation to changes in accessible surface areas of protein unfolding, *Protein Sci 4*, 2138-2148.
32. Sanchez, I. E., and Kiefhaber, T. (2003) Evidence for sequential barriers and obligatory intermediates in apparent two-state protein folding, *J Mol Biol 325*, 367-376.
33. Zlotnick, A., Johnson, J. M., Wingfield, P. W., Stahl, S. J., and Endres, D. (1999) A theoretical model successfully identifies features of hepatitis B virus capsid assembly, *Biochemistry 38*, 14644-14652.
34. Chemes, L. B., Noval, M. G., Sanchez, I. E., and de Prat-Gay, G. Folding of a cyclin box: linking multitarget binding to marginal stability, oligomerization, and aggregation of the retinoblastoma tumor suppressor AB pocket domain, *J Biol Chem 288*, 18923-18938.
35. Tsytlonok, M., and Itzhaki, L. S. The how's and why's of protein folding intermediates, *Arch Biochem Biophys 531*, 14-23.
36. Reimer, U., Scherer, G., Drewello, M., Kruber, S., Schutkowski, M., and Fischer, G. (1998) Side-chain effects on peptidyl-prolyl cis/trans isomerisation, *J Mol Biol 279*, 449-460.
37. Brandts, J. F., Halvorson, H. R., and Brennan, M. (1975) Consideration of the Possibility that the slow step in protein denaturation reactions is due to cis-trans isomerism of proline residues, *Biochemistry 14*, 4953-4963.
38. Kiefhaber, T., Quaas, R., Hahn, U., and Schmid, F. X. (1990) Folding of ribonuclease T1. 1. Existence of multiple unfolded states created by proline isomerization, *Biochemistry 29*, 3053-3061.
39. Kiefhaber, T., and Schmid, F. X. (1992) Kinetic coupling between protein folding and prolyl isomerization. II. Folding of ribonuclease A and ribonuclease T1, *J Mol Biol 224*, 231-240.
40. Smal, C., Alonso, L. G., Wetzler, D. E., Heer, A., and de Prat Gay, G. (2012) Ordered self-assembly mechanism of a spherical oncoprotein oligomer triggered by zinc removal and stabilized by an intrinsically disordered domain, *PLoS One 7*, e36457.

TABLES

Table 1 Observed rate constants obtained from refolding experiments at 1.0 M Gdm.Cl**.**

	constant (s^{-1})	error (s^{-1})
k_1	0.7451	3.33×10^{-2}
k_2	0.1604	7.07×10^{-3}
k_3	0.0434	2.34×10^{-3}
k_4	0.0093	3.68×10^{-4}
k_5	0.0019	2.70×10^{-5}

FIGURE LEGENDS

Figure 1. NS1 Unfolding kinetics. Unfolding kinetics of native NS1 protein diluted ten-fold to a final concentration of 8 μM, following changes in Far UV-CD and fluorescence signals at 5.0 Gdm.Cl concentration. The far –UV CD signal was followed at 216 nm and the fluorescence signal was followed at 325 nm. Traces were fit to a mono exponential function (continuous line) with residuals from the fit shown below the graph. The observed rate constants obtained from fitting were: $(1.80 \pm 0.2) \times 10^{-3}$ s^{-1}, from fluorescence experiments; and $(1.6 \pm 0.2) \times 10^{-3}$ s^{-1} from CD experiments.

Figure 2. Amplitude analysis for NS1 unfolding. Initial (t = 0, triangles) and final (t = ∞, filled circles) signals from kinetic unfolding experiments followed by fluorescence (A) or

CD signal at 216 nm (A). In both graphs final signals were calculated as the end point of exponential fits, while initial values were calculated as the difference between the end point values and the total amplitudes from all phases obtained in data fitting. The data from equilibrium unfolding experiments reported in ((*28*)) followed by the Trp fluorescence center of spectral mass (CSM) or by Far UV-CD signal at 216 nm are shown superimposed on amplitude data in panels A and B, respectively (○).

Figure 3. Chevron Plot for NS1 folding. Gdm.Cl dependence of the rate constants from unfolding and refolding experiments (chevron plot) shown in Figures 1 and 2 and Supplementary Figures 1-5. The rate constants corresponding to the unfolding phase from fluorescence measurements are represented as black circles for fluorescence measurements and as grey circles for CD measurements. The five observed refolding phases obtained by global data fitting are shown in the refolding side of the plot from 0 to 3.5M Gdm.Cl concentration (▽, ▼, △, ▲, □). The continuous line represents a linear fit of the unfolding phase from 5.0 to 7.0 M GdmCl. k_u was obtained from extrapolation of the value of ln k_u at 0 M Gdm.Cl obtaining a value of 2.5 ± 0.5 $\cdot 10^{-4}$ s^{-1}, and $m_u^{\ddagger}$ was obtained from the slope of the graph multiplied by RT (0.582 kcal·mol^{-1}) obtaining a value of 0.24 ± 0.02 kcal·$mol^{-1}\cdot M^{-1}$. The discontinuous line represents the predicted linear fit for the major refolding phase, obtained by assuming a two-state folding model (see Equations 4 and 5 from "Materials and Methods") which yielded a value of 3860 ± 850 s^{-1} for k_f and -2.26 ± 0.20 kcal·$mol^{-1}\cdot M^{-1}$ for $m_f^{\ddagger}$.

Figure 4. NS1 Refolding kinetics. Unfolded NS1 was rapidly mixed in buffer to a final

concentration of 1 M Gdm.Cl and the Trp fluorescence intensity change was monitored. **(**A) NS1 refolding kinetics followed by stopped-flow. The final protein concentration was 6 μM (B) Refolding kinetics followed by manual mixing. The final protein concentration was 8 μM The mixing dead time of the experiment was 15 s. For both experiments traces were fitted to mono, double and triple exponential functions (discontinuous line), with residuals for each fit shown below each trace. The observed rate constants for panel A were: k_1 (1.5 ± 0.1) s^{-1}, k_2 (0.32 ± 0.01) s^{-1} and k_3 (7.0 ± 0.3) x 10^{-2} s^{-1}; for panel B the observed rate constants were: k_4 (3.8 ± 0.2) x 10^{-2} s^{-1}, k_5 (8.5 ± 0.5) x 10^{-3} s^{-1} and k_6 (1.9 ± 0.1) x 10^{-3} s^{-1}.

Figure 5. Kinetics of NS1SOs formation by Temperature Jump. (A) Oligomerization kinetics were measured after transferring concentrated native NS1 from 4 ºC to buffer equilibrated at 47 ºC, and following changes in the far UV-CD signal at 216 nm (black dots) and in ThT fluorescence (discontinuous line) in two independent experiments. The final NS1 concentration in both experiments was 10 μM. The inset shows the far-UV CD spectra of native NS1 (continuous line) and NS1SOs at the end point of the experiment (discontinuous line). (B) Native NS1 held at 4 ºC was transferred to a cell holder maintained at 40 ºC at a final concentration of 17 μM and the resulting kinetics were measured by following changes in the particle size diameter by DLS (○) and by following the increase in ThT fluorescence (black line) in two independent experiments. The inset shows the particle size distribution, measured by DLS of initial and final species.

Figure 6. Kinetics and concentration dependence of NS1 self-assembly. (A) Normalized ThT fluorescence signals at NS1 protein concentrations ranging from 2.5 to 10 μM (bottom

to top). The grey area indicates the range of time points used for nucleus size analysis. (B) log-log plot of NS1SOs concentration as a function of monomeric NS1 concentration. Each dataset of values was calculated using data from all protein concentration at different time points within the grey zone demarked in plot (B): 200 s (●), 300 s (◊), 400 s (■), 500 s (△) and 600 s (▼). The nucleus size (2.3 ± 0.3) was calculated as an average of the slopes obtained for each data set according to Equation 7 (see Materials and Methods). (C) The reaction order for NS1SOs formation was calculated from the slope of the power dependence of the elongation rate as a function of NS1 total concentration according to Equation 8 (see Materials and Methods), obtaining a value of 1.10 ± 0.06.

Figure 7. Double Temperature-Jump experiments. (A) Native NS1 held at 4ºC was transferred to buffer equilibrated at 47 ºC at a final concentration of 12 μM. At different times points from 50 to 2000 seconds, the samples were transferred to a cell holder equilibrated at 20 ºC and the ensuing kinetics were measured following changes in the Far UV-CD ellipticity. In a similar experiment, NS1 oligomer formation was detected by size exclusion chromatography (Figure 8). (B) Oligomerization kinetics measured by Far UV-CD ellipticity at 220 nm (white dots). The continuous lines at 50, 320, 480 and 1120 seconds represent the changes in the far UV-CD signal kinetics when transferring from 47 to 20 ºC.

Figure 8. Reversible stage in oligomer formation determined by Double Temperature-Jump. (A) Far UV-CD spectra for samples from Figure 7: Native NS1 (full line), and samples measured at the end point of the kinetics after cooling at 20 ºC at 50 (dashed line)

480 (dashed and dotted line) and 1120 (dotted line) seconds. (B) Size exclusion chromatography (SEC) of samples heated at 47 ºC and cooled at different time points (between 50 and 2000 s) of the oligomerization process, as shown in Figure 7. SEC oligomerization experiments were performed after cooling at 20 ºC. The void volume of the column was 8.0 ml and the expected elution volume for a 15.5 KDa protein according to a calibration with protein standards is 13.0 ml. (C) Maximum observed absorbance values at 220 nm of particles eluted in the void volume in panel C (clear circles) superimposed to the ThT fluorescence increase (black line).

Figure 9. Minimal model for NS1 folding and NS1SOs formation. The diagram represents the proposed minimal model for NS1 folding and oligomerization, where U_{Slow} are unfolded polypeptides with non-native Xaa-prolyl isomers (filled circles), $U_{Fast,}$ is the unfolded polypeptide chain with native Xaa-prolyl isomers (empty circles) and N is the native NS1 monomer. In the polymerization reaction, M^* represents a native-like monomer and M_2^* is the dimeric nucleus for formation of the NS1 spherical oligomers (NS1SOs) which proceeds through monomer addition to the dimeric nucleus. In the model, two-way arrows indicate reversible processes while one-way arrows indicate irreversible reactions. The half times for folding, unfolding and oligomer formation obtained from kinetic analysis are reported in the scheme.

FIGURES

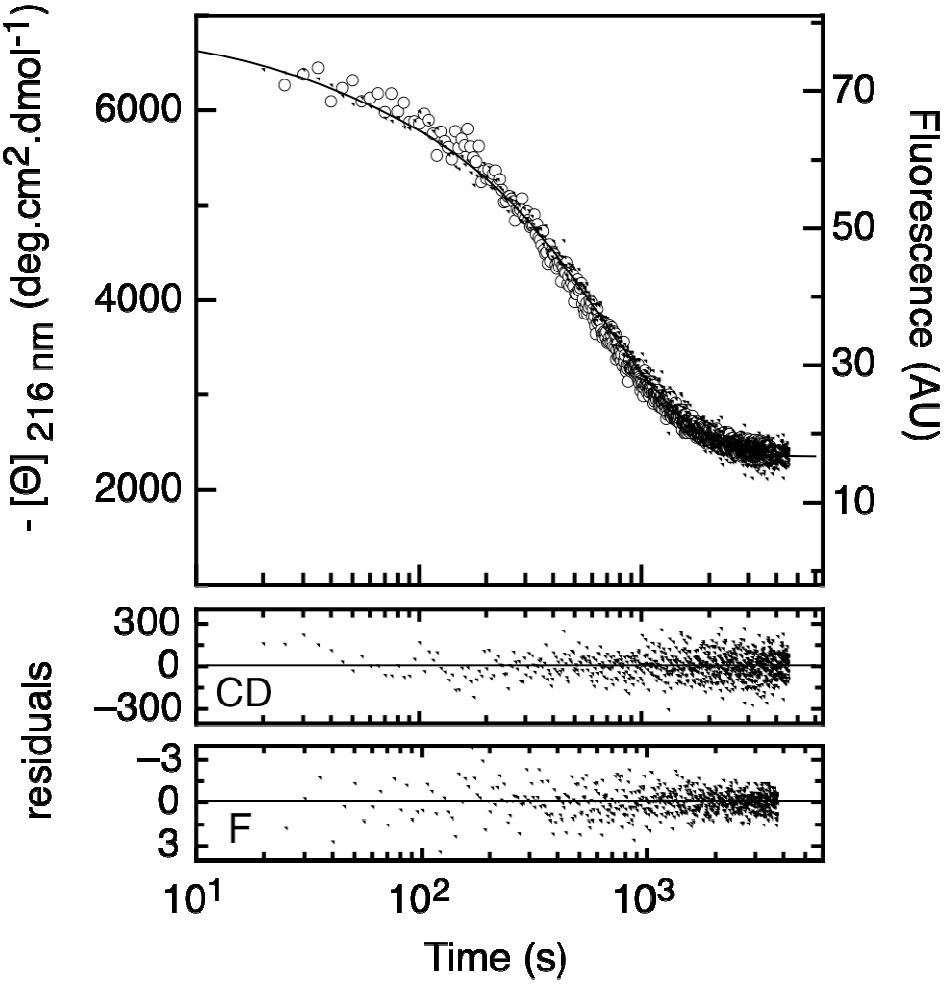

FIGURE 1

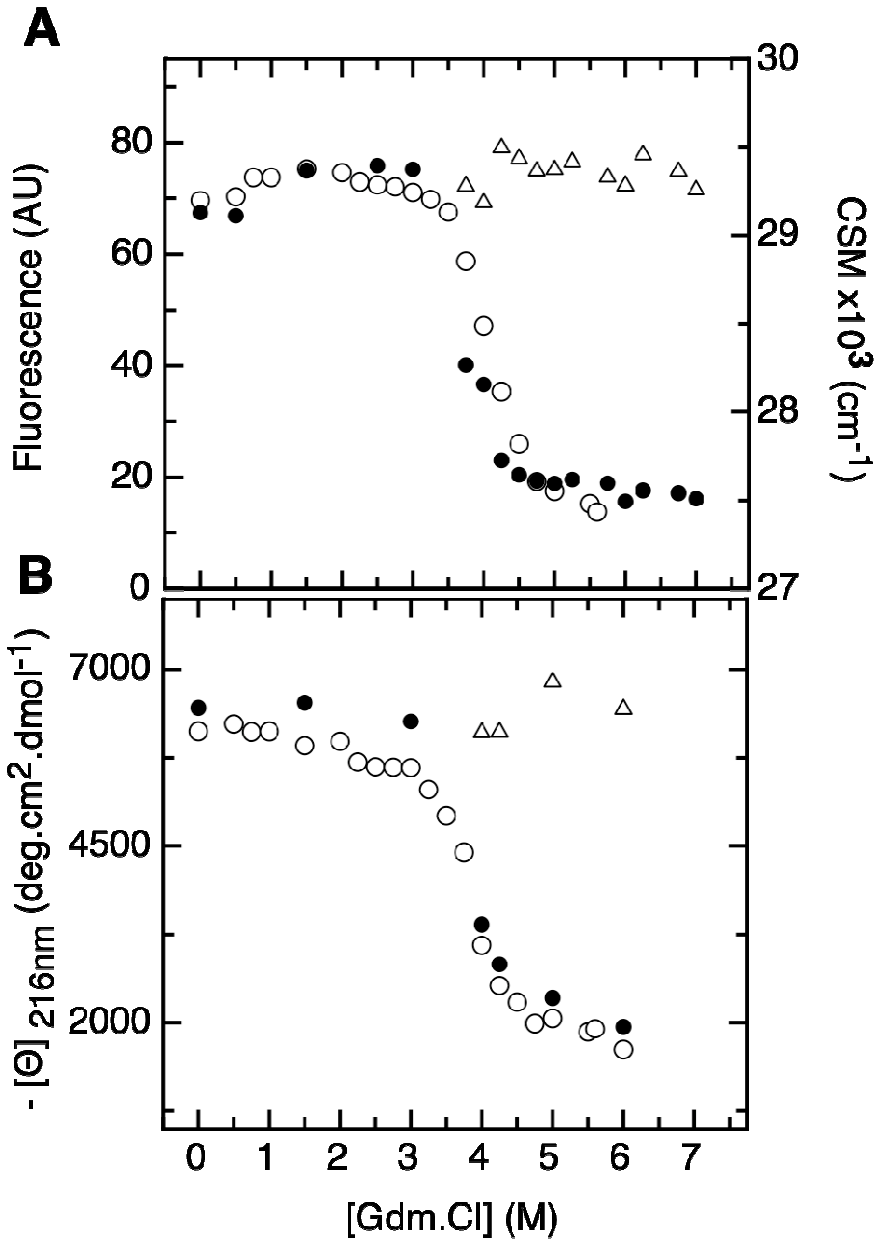
A
B
Fluorescence (AU)
CSM x10³ (cm⁻¹)
- [Θ] 216nm (deg.cm².dmol⁻¹)
[Gdm.Cl] (M)
0
20
40
60
80
27
28
29
30
2000
4500
7000
0
1
2
3
4
5
6
7

FIGURE 2

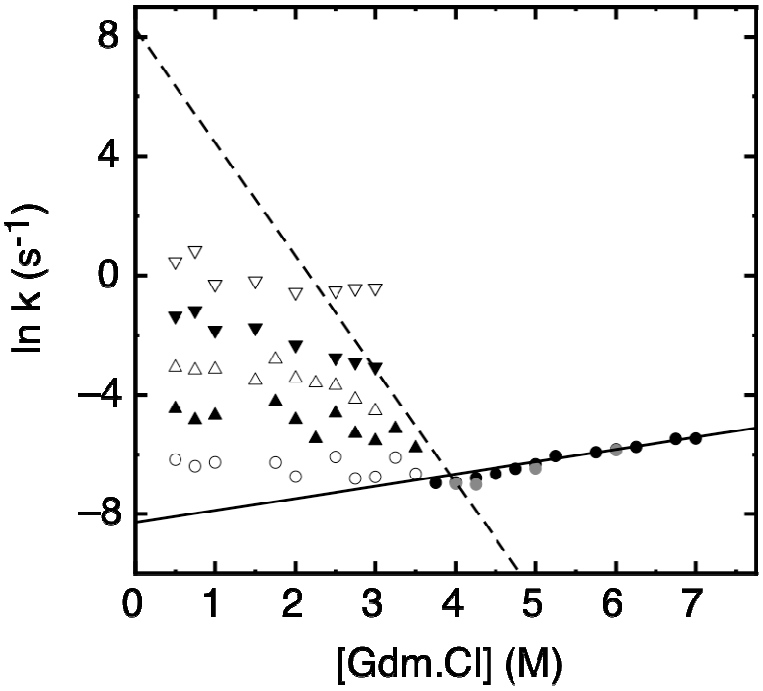

FIGURE 3

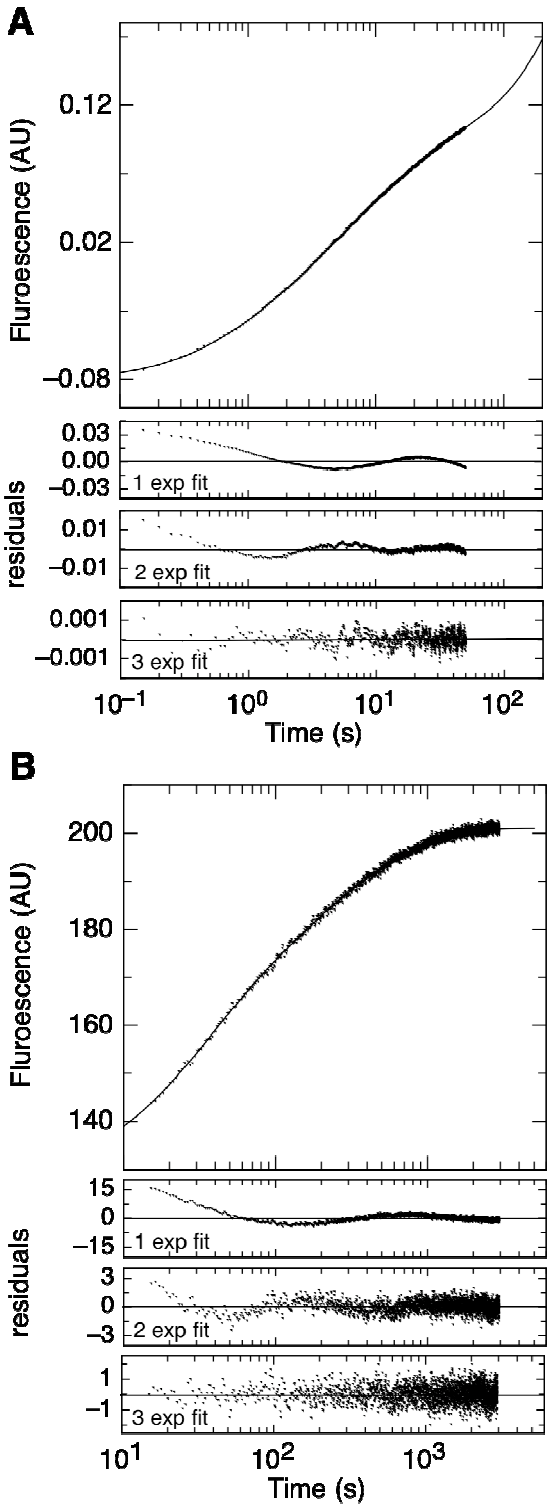
A
Fluroescence (AU)
0.12
0.02
−0.08
residuals
0.03
0.00
−0.03
1 exp fit
0.01
−0.01
2 exp fit
0.001
−0.001
3 exp fit
10−1
10^0
10^1
10^2
Time (s)
B
Fluroescence (AU)
200
180
160
140
residuals
15
0
−15
1 exp fit
3
0
−3
2 exp fit
1
−1
3 exp fit
10^1
10^2
10^3
Time (s)

FIGURE 4

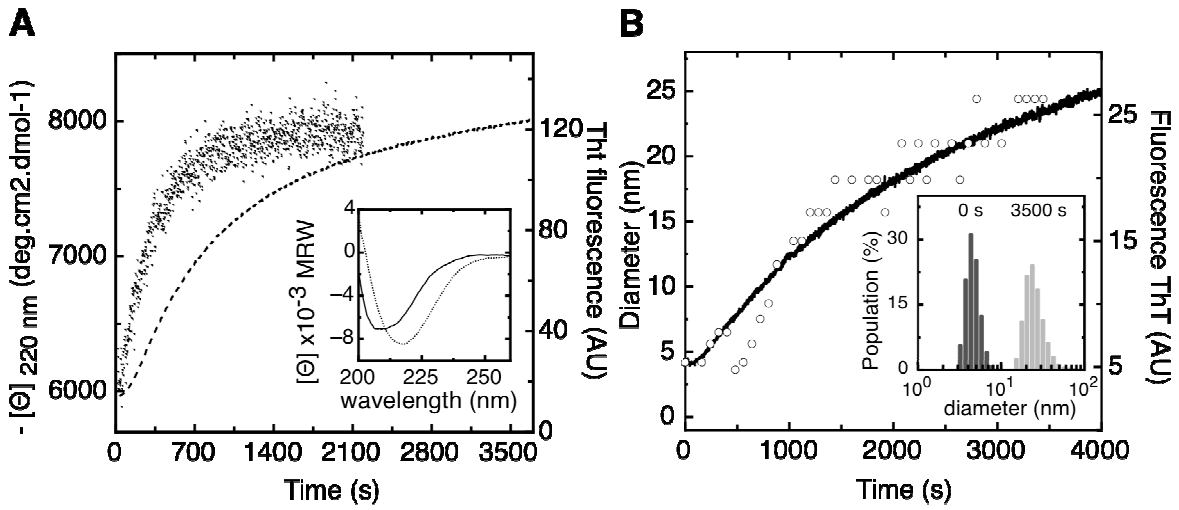
A
- [Θ] 220 nm (deg.cm2.dmol-1)
8000
7000
6000
0
700
1400
2100
2800
3500
Time (s)
120
80
40
0
Tht fluorescence (AU)
[Θ] x10-3 MRW
4
0
−4
−8
200
225
250
wavelength (nm)
B
Diameter (nm)
25
20
15
10
5
0
0
1000
2000
3000
4000
Time (s)
25
15
5
Fluorescence ThT (AU)
Population (%)
30
15
0
0 s
3500 s
10^0
10^1
10^2
diameter (nm)

FIGURE 5

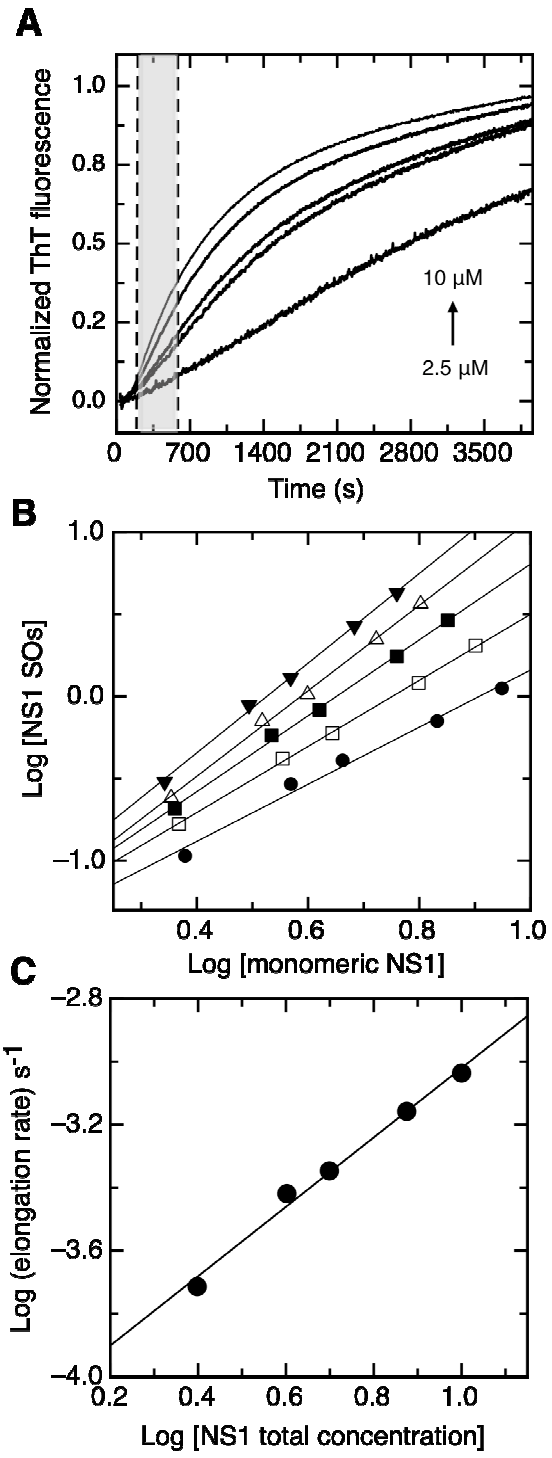
A
Normalized ThT fluorescence
1.0
0.8
0.5
0.2
0.0
10 μM
2.5 μM
0
700
1400
2100
2800
3500
Time (s)
B
Log [NS1 SOs]
1.0
0.0
−1.0
0.4
0.6
0.8
1.0
Log [monomeric NS1]
C
Log (elongation rate) s-1
−2.8
−3.2
−3.6
−4.0
0.2
0.4
0.6
0.8
1.0
Log [NS1 total concentration]

FIGURE 6

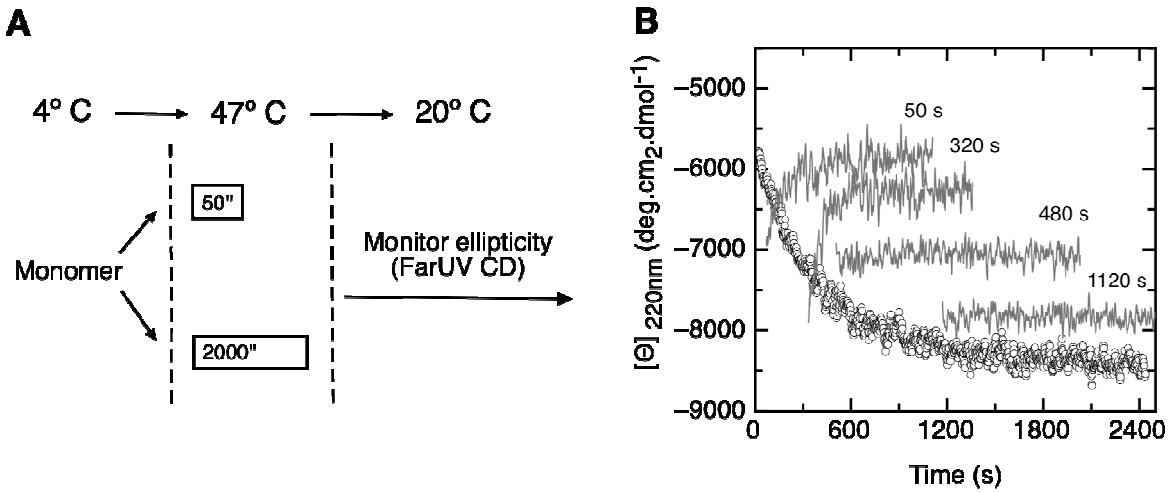
A
4° C
47° C
20° C
50"
Monomer
2000"
Monitor ellipticity
(FarUV CD)
B
50 s
320 s
480 s
1120 s
−5000
−6000
−7000
−8000
−9000
0
600
1200
1800
2400
Time (s)
[Θ] 220nm (deg.cm2.dmol−1)

FIGURE 7

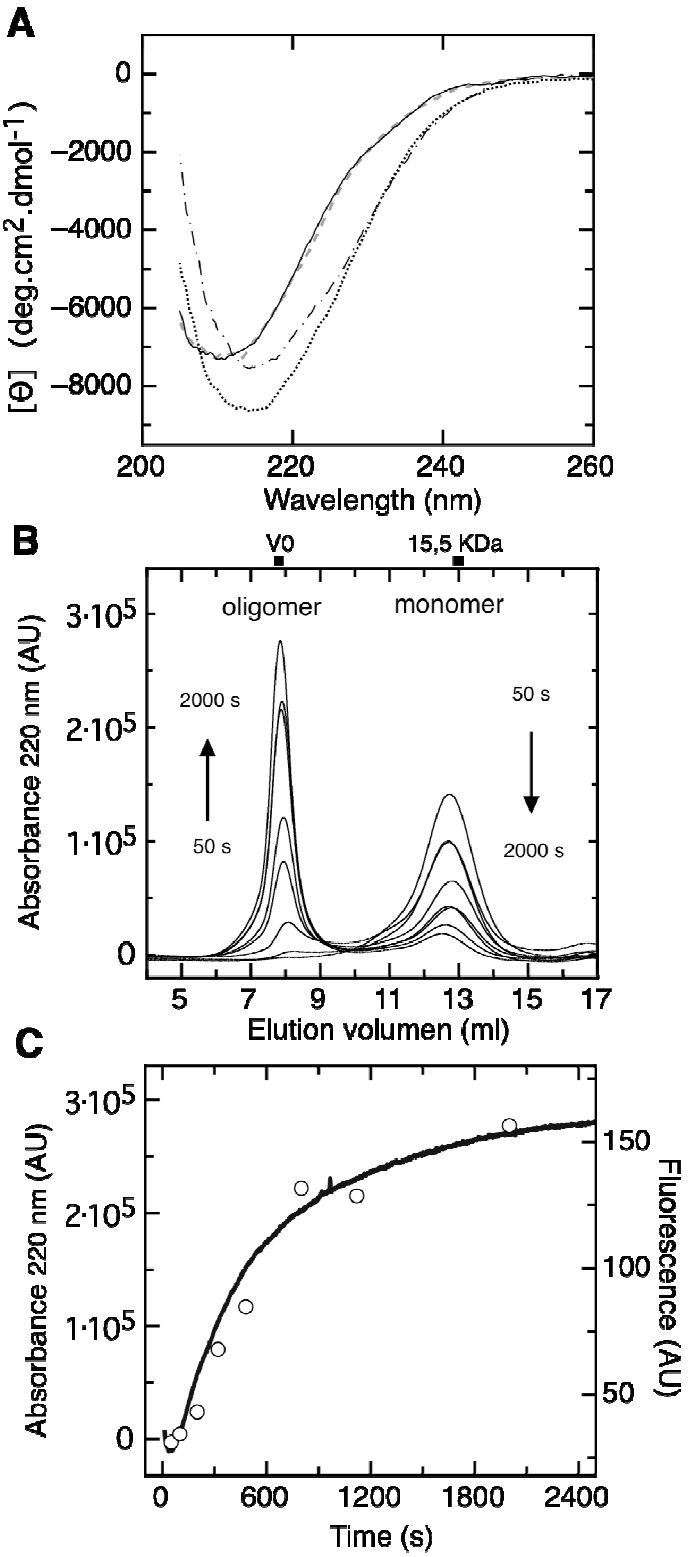
A
0
−2000
−4000
−6000
−8000
[Θ] (deg.cm2.dmol-1)
200
220
240
260
Wavelength (nm)
B
V0
15,5 KDa
oligomer
monomer
2000 s
50 s
50 s
2000 s
3·10^5
2·10^5
1·10^5
0
Absorbance 220 nm (AU)
5
7
9
11
13
15
17
Elution volumen (ml)
C
3·10^5
2·10^5
1·10^5
0
Absorbance 220 nm (AU)
150
100
50
Fluorescence (AU)
0
600
1200
1800
2400
Time (s)

FIGURE 8

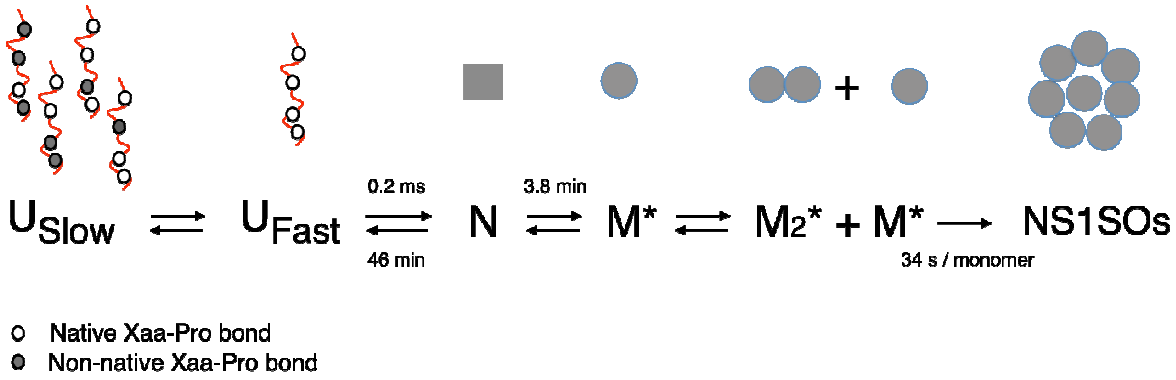
0.2 ms
3.8 min
U_{Slow}
U_{Fast}
N
M*
M_2* + M*
NS1SOs
46 min
34 s / monomer
Native Xaa-Pro bond
Non-native Xaa-Pro bond

FIGURE 9

GRAPHIC FOR TABLE OF CONTENTS

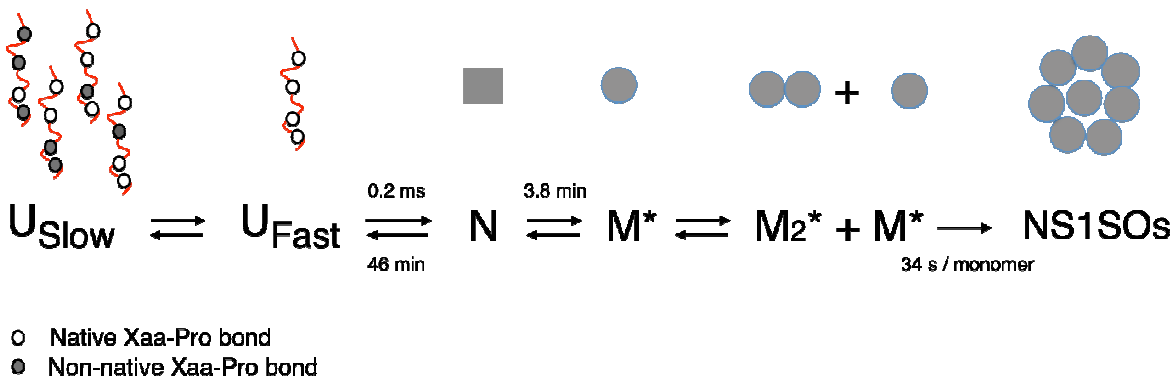

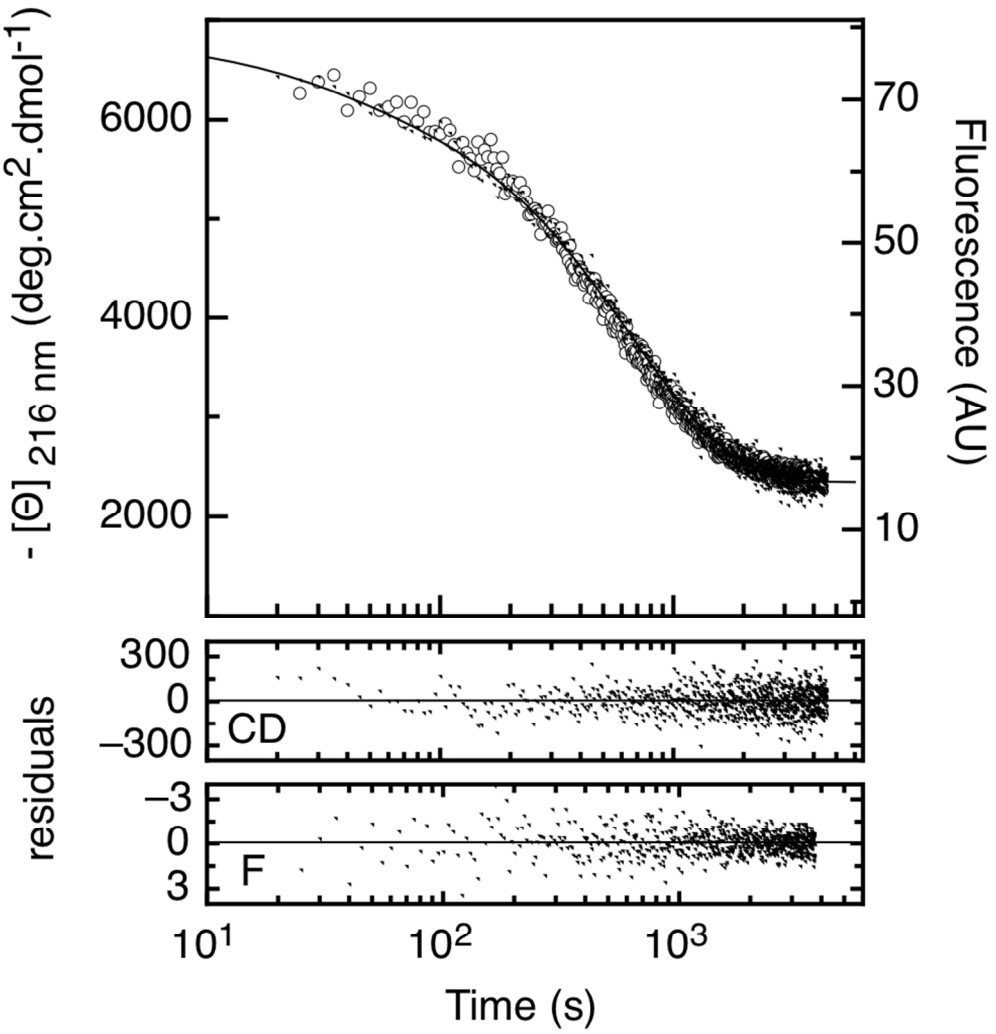

83x88mm (300 x 300 DPI)

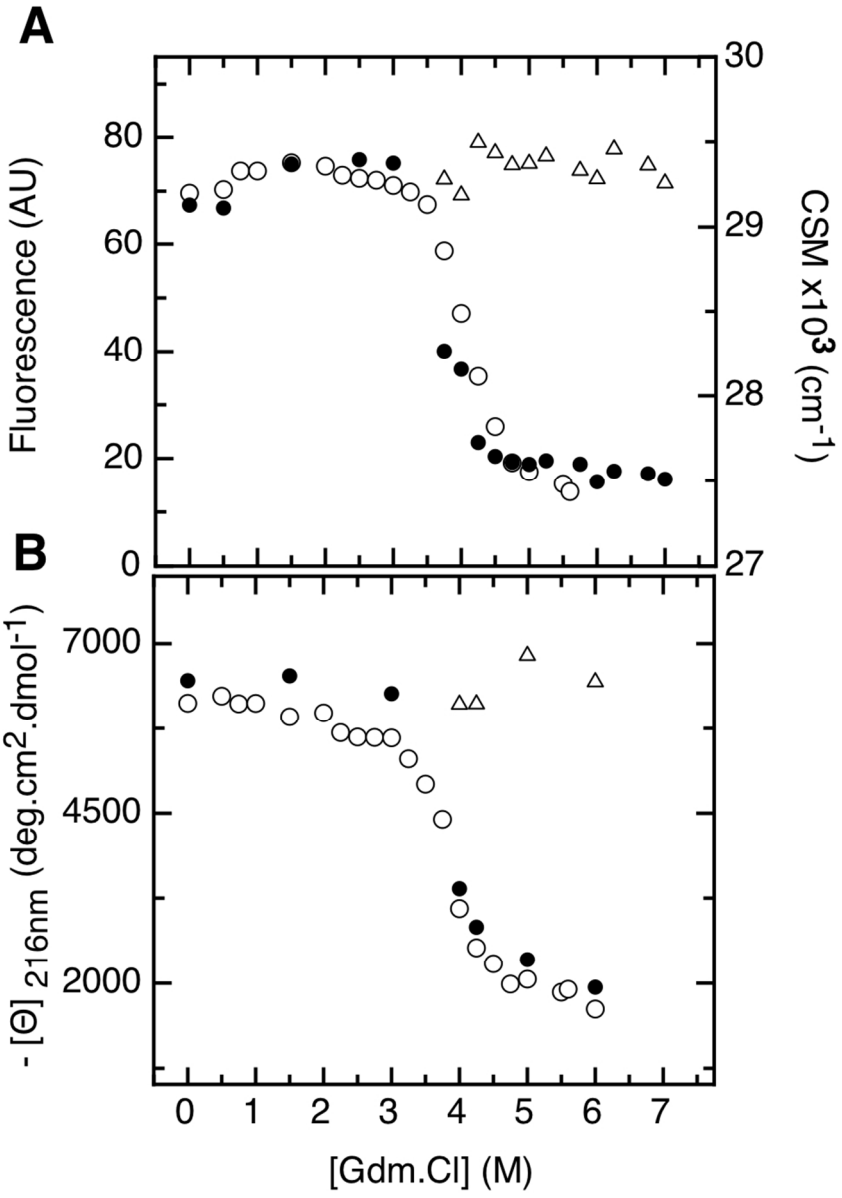

83x117mm (300 x 300 DPI)

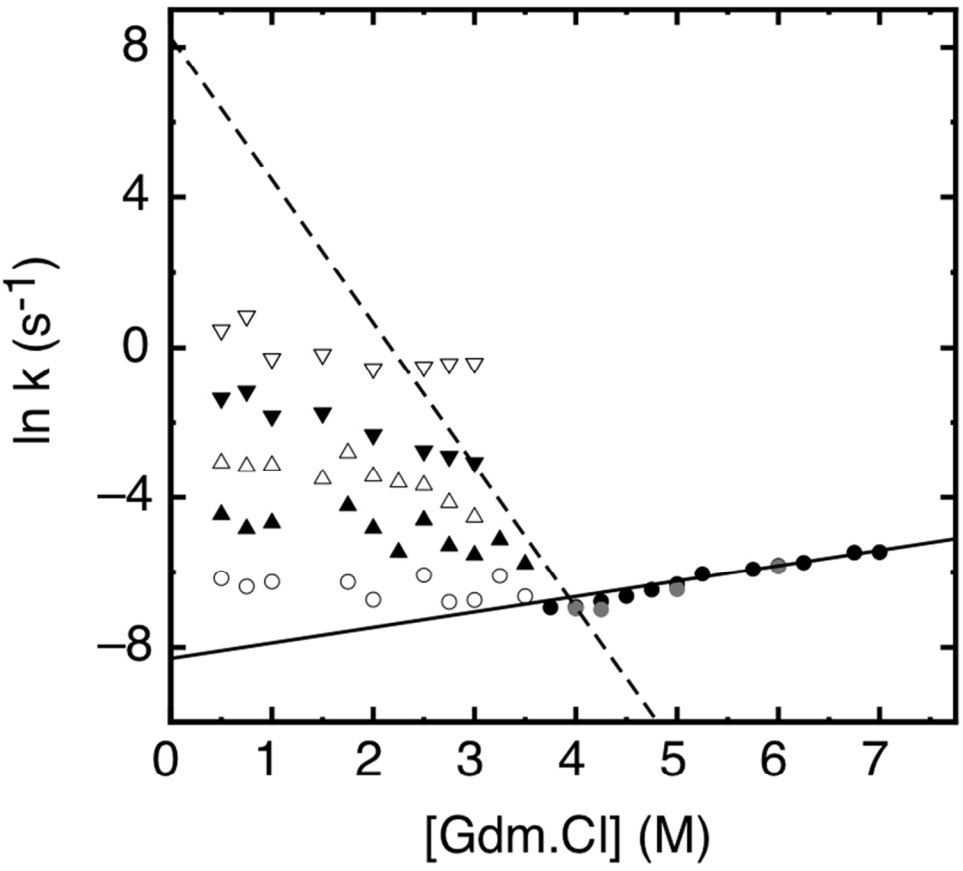

83x76mm (300 x 300 DPI)

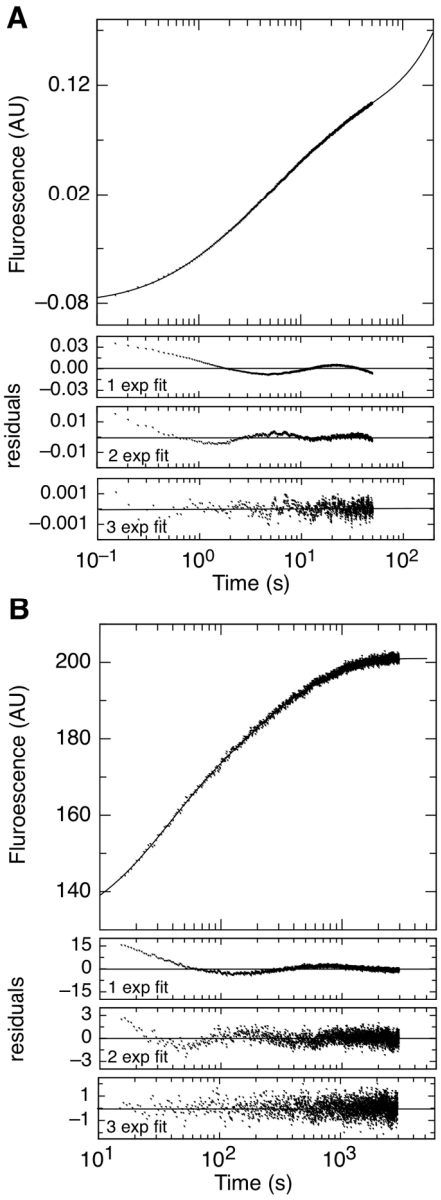

83x221mm (300 x 300 DPI)

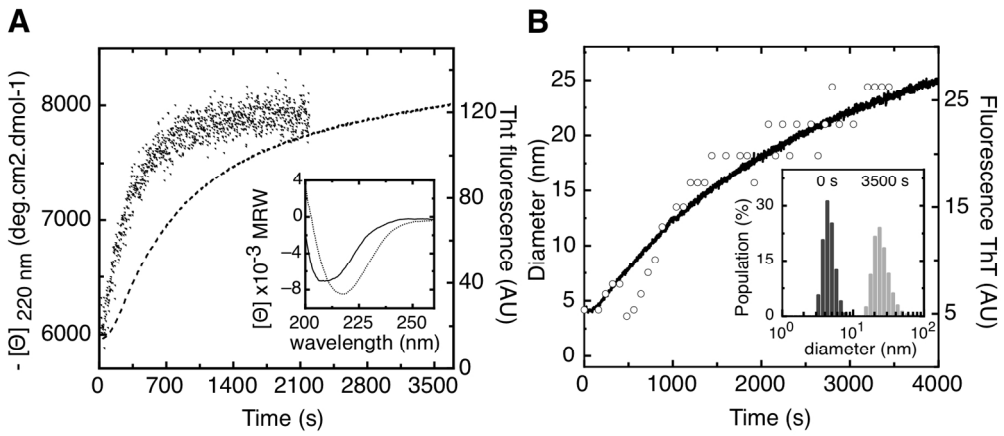

155x67mm (300 x 300 DPI)

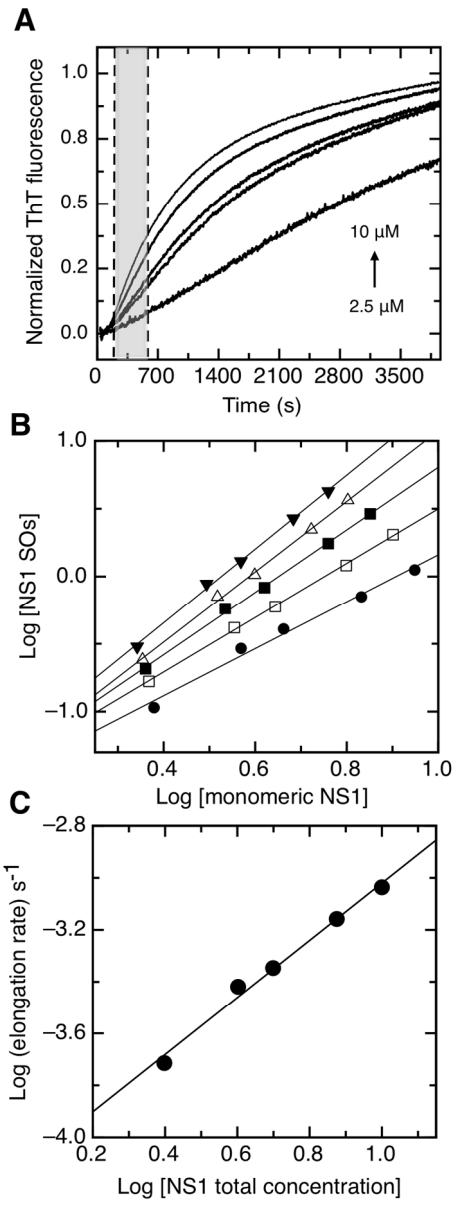

83x219mm (300 x 300 DPI)

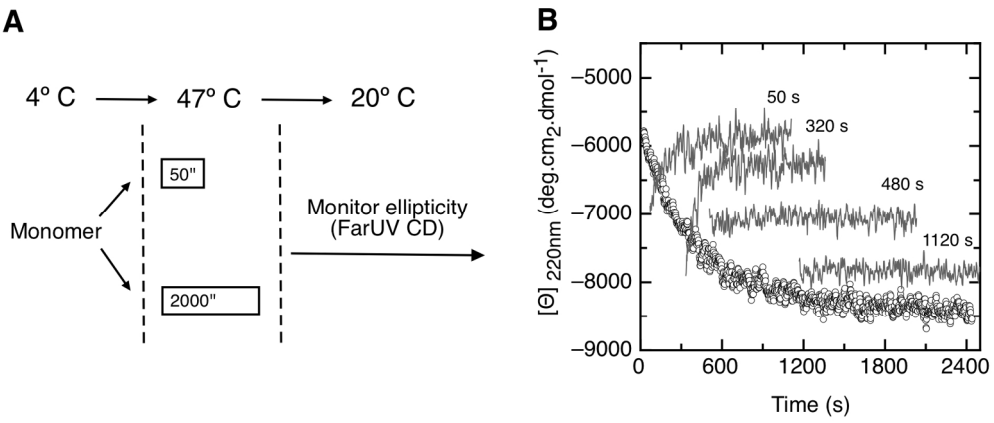

162x67mm (300 x 300 DPI)

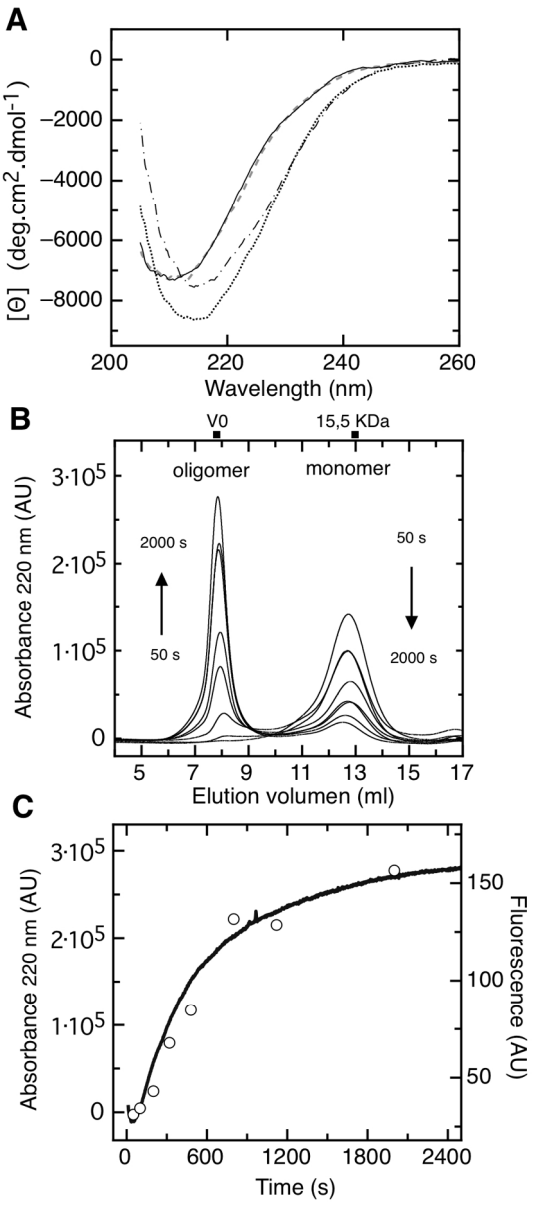

84x190mm (300 x 300 DPI)

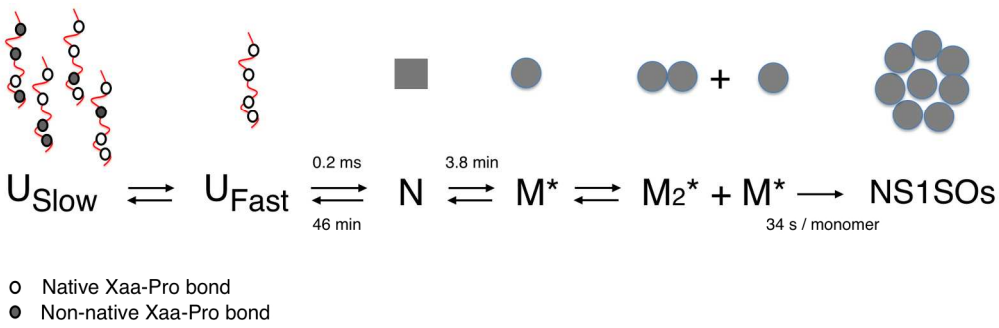

173x55mm (300 x 300 DPI)